

CsI-Antisolvent Adduct Formation in All-Inorganic Metal Halide Perovskites

Taylor Moot, Ashley R. Marshall, Lance M. Wheeler, Severin N. Habisreutinger, Tracy H. Schloemer, Caleb C. Boyd, Desislava R. Dikova, Gregory F. Pach, Abhijit Hazarika, Michael D. McGehee, Henry J. Snaith, and Joseph M. Luther*

The excellent optoelectronic properties demonstrated by hybrid organic/inorganic metal halide perovskites are all predicated on precisely controlling the exact nucleation and crystallization dynamics that occur during film formation. In general, high-performance thin films are obtained by a method commonly called solvent engineering (or antisolvent quench) processing. The solvent engineering method removes excess solvent, but importantly leaves behind solvent that forms chemical adducts with the lead-halide precursor salts. These adduct-based precursor phases *control* nucleation and the growth of the polycrystalline domains. There has not yet been a comprehensive study comparing the various antisolvents used in different perovskite compositions containing cesium. In addition, there have been no reports of solvent engineering for high efficiency in all-inorganic perovskites such as CsPbI₃. In this work, inorganic perovskite composition CsPbI₃ is specifically targeted and unique adducts formed between CsI and precursor solvents and antisolvents are found that have not been observed for other A-site cation salts. These CsI adducts control nucleation more so than the PbI₂-dimethyl sulfoxide (DMSO) adduct and demonstrate how the A-site plays a significant role in crystallization. The use of methyl acetate (MeOAc) in this solvent engineering approach dictates crystallization through the formation of a CsI-MeOAc adduct and results in solar cells with a power conversion efficiency of 14.4%.

shown a higher level of tolerance to material and crystallization defects than any other optoelectronic semiconductor family. This has enabled fabrication of high-quality semiconductors from facile methods such as solution processing. As such, researchers have been able to demonstrate impressive performance in photovoltaic devices with single junction power conversion efficiency (PCE) exceeding 25% and tandem cell efficiency surpassing 28% under AM1.5G simulated sunlight.^[1,2] The combination of high performance and low-cost production is enabling perovskite solar cell commercialization.^[3,4] However, defect tolerance does not mean that any defects, commonly formed during film fabrication, are completely benign. One of the biggest breakthroughs in halide perovskites was the introduction of the solvent engineering approach, which produces high-quality, pinhole-free, device-grade thin films by taking advantage of specific precursor solvent interactions coupled with a nucleating antisolvent drip.^[5] This approach was first demonstrated with MAPbI₃ in 7:3 gamma-


butyrolactone (GBL):dimethyl sulfoxide (DMSO) using toluene as the antisolvent and has become a universal and reproducible method for many groups to achieve high efficiency perovskite

1. Introduction

Metal halide perovskites, ABX₃ (A = methylammonium (MA), formamidinium (FA) or Cs; B = Pb or Sn; X = I, Br, Cl) have

Dr. T. Moot, Dr. L. M. Wheeler, Dr. S. N. Habisreutinger, C. C. Boyd, D. R. Dikova, G. F. Pach, Dr. A. Hazarika, Prof. M. D. McGehee, Dr. J. M. Luther
National Renewable Energy Laboratory
Golden, CO 80401, USA
E-mail: Joey.Luther@NREL.gov
Dr. A. R. Marshall, Prof. H. J. Snaith
Department of Physics
University of Oxford
Oxford OX1 3PU, UK
Dr. T. H. Schloemer
Department of Chemistry
Colorado School of Mines
Golden, CO 80401, USA

C. C. Boyd
Department of Material Science and Engineering
Stanford University
Palo Alto, CA 94305, USA
D. R. Dikova
Department of Chemistry
University of Michigan
Ann Arbor, MI 48109, USA
Prof. M. D. McGehee
Department of Chemical and Biological Engineering
University of Colorado
Boulder, CO 80309, USA

 The ORCID identification number(s) for the author(s) of this article can be found under <https://doi.org/10.1002/aenm.201903365>.

DOI: 10.1002/aenm.201903365

solar cells using a variety of perovskite compositions, such as complex compositions commonly called the triple A-site cation formulation, which is $\text{Cs}_x\text{FA}_y\text{MA}_{1-x-y}\text{Pb}(\text{I}_2\text{Br}_{1-z})_3$.^[5–7] However, extending this approach toward other compositions requires insight into the various adducts formed between precursors and solvents, as well as the interaction between the perovskite film and the crystallization initiator (i.e. antisolvent).^[8,9]

While DMSO has always been considered a good solvent for hybrid Pb-halide perovskites, early on it was abandoned for dimethylformamide (DMF) because DMSO slows the crystallization, whereas DMF evaporates cleanly and rapidly, leading to films with better morphology.^[5,10,11] DMSO forms a strong adduct with PbI_2 which retards perovskite crystallization through first forming a MAI–DMSO– PbI_2 crystalline, “precursor” phase, which then converts to the 3D ABX_3 perovskite phase upon annealing.^[11] The solvent engineering method exploits this effect by using a mixture of DMF and DMSO to control the crystallization rate by tuning the solvent ratio and thus the amount of PbI_2 –DMSO complex. An antisolvent quench is also incorporated to intentionally control the exact nucleation time through the introduction of an antisolvent that supersaturates the precursor solution and removes excess precursor solvent.^[5,12–14] The antisolvent quench must happen within a specific nucleation window since quenching too early will not cause supersaturation and quenching after the film has already begun to nucleate will not induce the ideal nucleation site density.^[15–17] When the quenching occurs within this window, heterogeneous nucleation is promoted at the initial crystallization stage and minimizes pinholes in the resulting films.^[9,13] By controlling nucleation and slowing down the crystallization, the perovskite films have more uniform film coverage.

Although the use of solvent controlled crystallization has been used for many perovskite compositions, a fundamental understanding of how this mechanism works for all compositions is lacking. High-efficiency perovskite solar cells utilizing the triple cation formulation have been shown to have PCE exceeding 20%, low radiative loss, and stability for thousands of hours under certain stressing conditions.^[6,18,19] CsI is incorporated to improve both film quality and stability, often through minimizing I/Br halide phase segregation under illumination, which is critical for use in high-performance perovskite tandems.^[20–24] The precursor solutions to create such films contain many salts that may interact in various ways. Recent reports have shown that the introduction of low amounts of CsI (<15%) further retards crystallization in mixed cation perovskites because more DMSO stays in the as-cast, preannealed film, resulting in higher quality films following crystallization.^[25] Additionally, the introduction of CsI lowers the formation energy of the cubic perovskite phase as compared to intermediate phases thus promoting crystallization directly to the 3D ABX_3 perovskite phase.^[26]

Although PbX_2 –DMSO complexes have been known for decades, it is unclear how CsI will interact with the solvents, and hence might impact crystallization at higher concentrations. For the most commonly used wide-bandgap perovskites, $\text{FA}_x\text{Cs}_{1-x}\text{Pb}(\text{I}_y\text{Br}_{1-y})_3$, typically up to 30% Cs is utilized, although up to 50% Cs has been reported.^[22,27–29] In applications where higher temperature operation may be experienced

or perhaps when organic outgassing is a concern, such as operation in space, all-inorganic perovskites may prove to be the most useful. Notably, there are no reports of all-inorganic CsPbI_3 perovskites fabricated with traditional antisolvents, and only one report which utilized an air-drying method.^[30] There has been work on controlling crystallization dynamics by the introduction of additives such as hydroiodic acid (HI), through templating growth with MAI or Cs_4PbI_6 , or by the use of $\text{DMA}_{0.3}\text{Cs}_{0.7}\text{PbI}_3$ with an antisolvent.^[31–37] Based on the success of the antisolvent technique in mixed A-site perovskites, it is noteworthy that there are no reports of antisolvents used for pure CsPbI_3 perovskites, particularly given that the proposed crystallization mechanism ignores any influence of the A-site and is based primarily on PbI_2 –DMSO interactions. This suggests that there is an incomplete understanding of the CsI influence on crystallization and how to control it.

Here, we probe the crystallization mechanism for CsPbI_3 and identify methyl acetate as an effective antisolvent. By studying the film adduct chemistry, crystal structure, morphology and optoelectronic properties, we demonstrate that CsI complexes strongly with DMSO and can fully retard any crystallization. Traditional antisolvents, such as toluene or chlorobenzene, do not promote heterogeneous nucleation and only antisolvents that form an adduct with CsI promote heterogeneous nucleation and high-quality films. The implications of the CsI complexes are critical to all-inorganic perovskites as well as for the mixed cation perovskites, which are the most stable perovskites.

2. Results and Discussion

The requirements for an appropriate antisolvent are to evaporate quickly and be miscible with DMSO and DMF, but poorly solvate the perovskite salts. However, the exact antisolvent mechanism and preferred physical and/or chemical properties necessary are unclear. Here, we explore six different antisolvents chosen to fully cover the basis of relevant solvent parameters: boiling point, vapor pressure, polarity (Hansen polar parameter or Gutmann's donor number), and miscibility (Hildebrand parameter) (Table S1, Supporting Information). Comparison between no antisolvent (untreated) and the six other antisolvents allows us to glean the effect of DMSO and the antisolvent influence on nucleation of CsPbI_3 . Between the antisolvents, chlorobenzene (CB) and toluene (Tol) represent the traditional nonpolar antisolvents, diethyl ether (DEE), and anisole help in understanding of the influence of solvent removal rate based on differences in boiling point and vapor pressure, and ethyl acetate (EtOAc) and methyl acetate (MeOAc) probe whether the polarity of the antisolvent aids in nucleation, since both are more polar than the traditional antisolvents.

To understand the crystallization dynamics and antisolvent mechanism of CsPbI_3 , the as-quenched films prior to annealing were first studied. It has previously been shown that the formation of a crystalline intermediate, typically light brown, precursor phase is critical in forming high-quality, pinhole-free films.^[15,38] Without an antisolvent, the CsPbI_3 as-quenched, preannealed film retains a yellow color with an absorption onset of 450 nm (Figure 1A). CB, Tol, and DEE do not change the as-quenched film from the yellow color (Figure 1C). The yellow

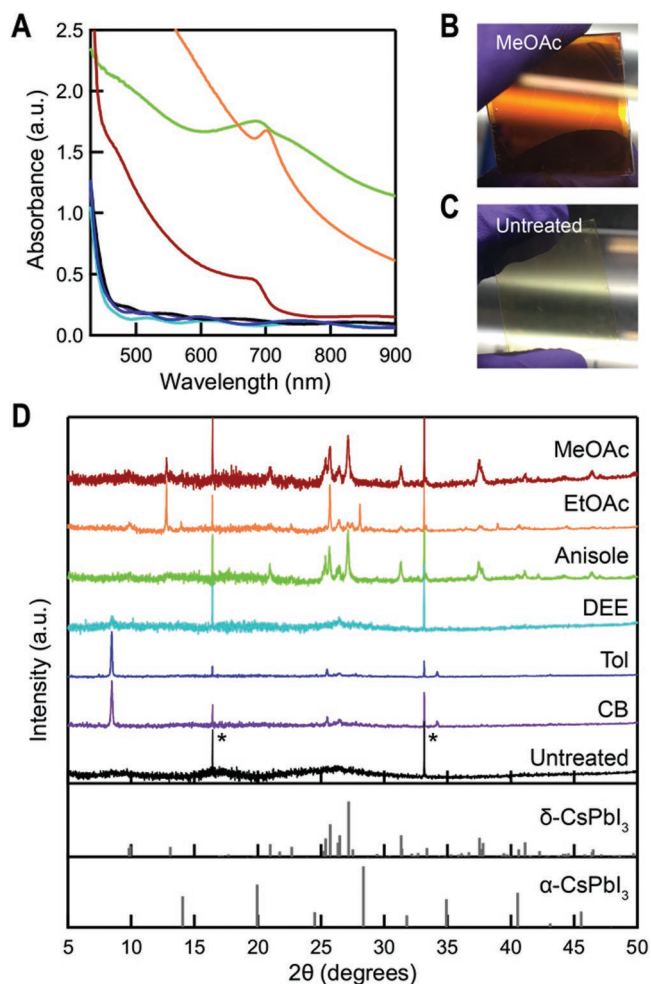


Figure 1. Analysis of as-quenched, preannealed films with various antisolvent treatments: Untreated (black), CB (purple), Tol (dark blue), DEE (turquoise), Anisole (green), EtOAc (orange) and MeOAc (red). A) UV-vis absorbance of as-quenched films, representative pictures of an B) MeOAc and C) untreated as-quenched film and D) XRD where * denotes quartz substrate peak and background amorphous peak from the air-free holder was subtracted out with the ICSD XRD pattern for δ -CsPbI₃, and α -CsPbI₃ (gray).

color persists regardless of antisolvent timing, suggesting that the nucleation window is not being missed (Figure S1, Supporting Information), although films eventually turn brown over tens of minutes as has been previously reported.^[30] Conversely, the use of anisole, EtOAc and MeOAc (Figure 1B) all turned the as-quenched CsPbI₃ film immediately to a brown color, with a bandgap of ≈ 1.72 eV, where EtOAc and anisole showed significant scattering backgrounds. 1.72 eV is the bandgap typically reported for the CsPbI₃ orthorhombic 3D perovskite phase and was obtained here at room temperature.^[20]

X-ray diffraction (XRD) of the untreated, preannealed films (Figure 1D) shows no crystalline peaks, which is in stark contrast to that of MAPbI₃, which crystallizes into the MAI-PbI₂-DMSO phase without any antisolvent treatment and has a strong peak at $\approx 10^\circ$ 2θ .^[5,11] Recent reports have demonstrated that CsI can retard crystallization in mixed A-site perovskites by forming a strong adduct with DMSO, and we see that

crystallization is completely stopped in neat CsPbI₃.^[25] The use of DEE as an antisolvent does not induce crystallization, whereas the other two yellow, as-quenched antisolvent treatments, CB and Tol, result in the crystallization of a CsI-PbI₂-DMSO adduct with peaks at 8.5° , 25.5° and 34° 2θ similar to MAI-PbI₂-DMSO previously reported.^[11] All three antisolvents that turned the as-quenched films brown, (anisole, EtOAc, and MeOAc) created films that show crystalline peaks between 25° and 27° 2θ , indicative of the δ -CsPbI₃ phase (Figure S2, Supporting Information). This is similar to what has been shown for the CsPbI₃ solvent-controlled growth method, where the dried films turned brown and showed both a nonperovskite and perovskite orthorhombic (δ) perovskite CsPbI₃ phases.^[30] However, despite the brown color seen here, we are unable to obtain XRD patterns that show any black perovskite phases (α , β , nor γ).

To further understand the formation, or lack thereof, of a crystalline precursor phase, the influence of solvent is probed. Previous reports that the CsI-DMSO interaction may slow down nucleation and the formation of a CsI-PbI₂-DMSO precursor phase suggest that the exact DMSO interaction between CsPbI₃ and the antisolvent is critical to nucleation and crystallization. Figure 2 shows the FTIR spectrum of each as-quenched film after exposing the sample to vacuum to remove unbound solvent and allow for study on the bound solvent species. None of the films changed appearance after the vacuum treatment. FTIR shows both residual DMF and DMSO at characteristic stretching modes of $\nu_{C=O}$ at ≈ 1660 cm^{-1} and $\nu_{S=O}$ at ≈ 1000 cm^{-1} , respectively, in each antisolvent film.^[38,39] It has been previously shown that both DMF and DMSO form adducts with perovskite precursors, albeit with different strengths.^[40–42]

To better quantify the residual DMSO and DMF, ¹H NMR was performed on as-quenched films by dissolving the films in deuterated DMSO-*d*₆. Films were first stored under rough vacuum for 3 min and then dissolved to allow us to focus on the bound solvent species instead of unbound species. The deuterated DMSO-*d*₆ quintet peak is at 2.50 ppm whereas the undeuterated DMSO singlet peak is slightly shifted at 2.54 ppm, allowing us to probe specifically the residual (undeuterated) DMSO in the as-quenched films.^[43] To quantitatively determine the PbI_x:DMSO ratio, the intensity of the undeuterated DMSO peak was normalized to the solution PbI_x absorbance (Figure 2B, Figure S3, Supporting Information). A small amount of DMF was found in each film and the values are all approximately the same regardless of antisolvent treatment (Table S2, Supporting Information). The residual DMF:DMSO ratio in the untreated, as-quenched film is $\approx 1:15$, in stark contrast to the starting 4:1 DMF:DMSO ratio. This suggests that evaporation during spincoating, not the antisolvent, removes most of the DMF. For comparison, the residual bound DMSO amount in each as-quenched film was then compared to the untreated film (Figure 2C) by normalizing to the DMSO NMR peak area in the untreated film. All antisolvent treatments removed at least some bound DMSO compared to the untreated film, demonstrating that the antisolvent is specifically targeting bound DMSO rather than excess solvent in general. However, there are no clear trends between color, crystal phase, and residual bound DMSO amount. DEE as-quenched films remain yellow and amorphous, akin to untreated films but have 66%

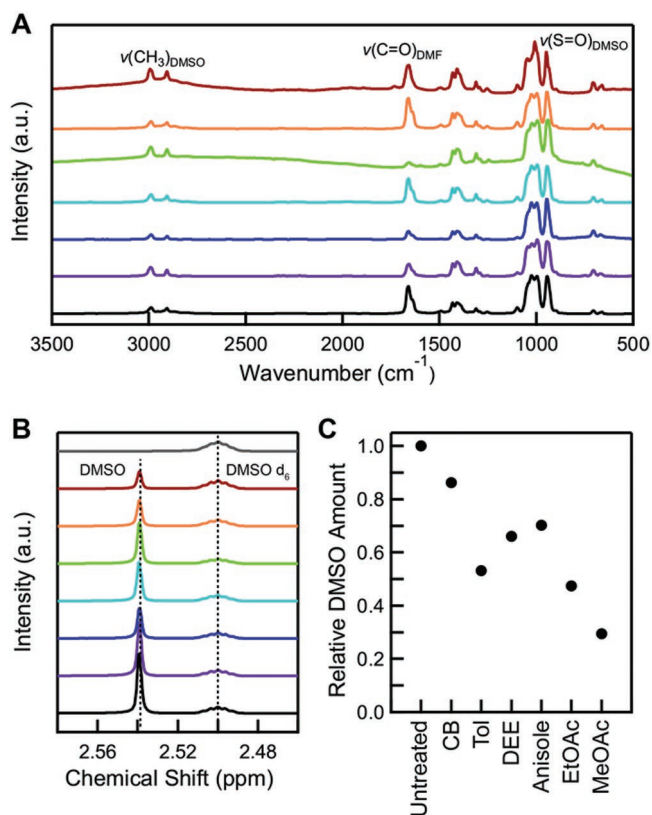


Figure 2. Characterization of residual bound DMSO and DMF in as-quenched untreated (black), CB (purple), Tol (dark blue), DEE (turquoise), anisole (green), EtOAc (orange), and MeOAc (red) films by A) FTIR and B) ^1H NMR, where gray is the DMSO- d_6 NMR solvent. C) Relative residual bound DMSO amount found in each as-quenched film normalized to the untreated DMSO amount.

residual bound DMSO. CB and Tol both form a PbI_2 -DMSO crystalline precursor phase but have large variabilities in the relative bound DMSO amounts at 86% and 53%, respectively. Anisole, EtOAc and MeOAc all form a brown, δ - CsPbI_3 crystalline precursor phase and also have large variabilities in the relative residual bound DMSO amounts. MeOAc has the lowest residual bound DMSO amount at 29%, but EtOAc has a similar residual bound DMSO amount to Tol at 47% as does anisole to DEE at 70%. Further, there are no clear trends between any of the typically cited solvent parameters (boiling point, vapor pressure, miscibility, polarity) and the degree of removal of DMSO (Figure S4, Supporting Information). This suggests that the typical ways of thinking about the antisolvent mechanism are inadequate for CsPbI_3 .

These antisolvent physical parameters specifically do not account for any sort of adduct formation such as PbI_2 -DMSO, which has been identified to strongly influence the crystallization dynamics in halide perovskites.^[15,40,42,44–48] Basicity scales like the Gutmann's donor notionally account for the strength of adduct formation, but is based on adduct formation with a model Lewis acid (SbCl_5) and does not account for hardness or softness of the constituents thus is incomplete.^[42] To probe adduct formation, FTIR was done on each as-quenched CsPbI_3 film, as well as as-quenched films where the precursor

contained only PbI_2 or CsI to deconvolute the exact species involved in adduct formation. Typically, the A-site is thought to be a passive bystander and not play a role in the adduct formation. A DMSO $\nu_{\text{S=O}}$ doublet at $\approx 975\text{ cm}^{-1}$ and DMF $\nu_{\text{C=O}}$ peak at $\approx 1660\text{ cm}^{-1}$ appear in both CsPbI_3 and PbI_2 untreated films (Figure 3A,B) as would be expected due to the known PbI_2 -DMSO adduct formation as well as the weaker PbI_2 -DMF adduct.^[5,38] Notably, there is also a clear narrow DMSO $\nu_{\text{S=O}}$ peak at 1030 cm^{-1} and a small DMF peak in the CsI film. The resulting CsPbI_3 DMSO peak appears to be a superposition of both the PbI_2 -DMSO and CsI -DMSO, confirming that the individual interactions of CsI and PbI_2 make up the adduct interaction for CsPbI_3 . The evidence here for a strong CsI -DMSO adduct demonstrates that CsI -DMSO, and more generally the A-site, can play an important role in the nucleation and crystallization dynamics and should not be ignored. Indeed, this correlates well with other observations that a CsI -DMSO interaction retards crystallization in mixed A-site perovskites and a DMSO-rich preannealed CsPbI_3 remains amorphous.^[25]

Further inspection of the CsI FTIR for the brown as-quenched films (anisole, EtOAc, MeOAc) shows additional peaks beyond DMF and DMSO, whereas the yellow as-quenched films (CB, Tol, DEE) only show DMF and DMSO (Figure 3C–H, Figure S5, Supporting Information). The MeOAc carbonyl group is evident in both the CsI and CsPbI_3 FTIR spectra at 1740 cm^{-1} , suggesting there is also a CsI -MeOAc adduct that is present in the as-quenched CsPbI_3 (Figure 3H).^[49] This MeOAc peak in CsI is slightly shifted from CsPbI_3 -MeOAc at 1730 cm^{-1} and shifted far from the neat MeOAc peak at 1770 cm^{-1} , again indicative of complexation (Figure S5, Supporting Information).^[49] Similarly, the anisole phenyl group stretch at $\approx 1600\text{ cm}^{-1}$ is evident in both CsI and CsPbI_3 and the EtOAc carbonyl doublet at $\approx 1730\text{ cm}^{-1}$ is only evident in the CsI FTIR spectra (Figure 3F,G). This demonstrates that anisole, EtOAc, and MeOAc act as antisolvents in the traditional sense by removing bound solvent, yet also form adducts making them a specific type and subset of antisolvents, an adduct antisolvent. We note that the formation of CsI -antisolvent adducts does not directly correlate with any solvent parameter, such as polarity or Gutmann's donor number, and CsI -acetate adducts have been previously reported in CsPbI_3 quantum dots (QDs).^[50,51] Each antisolvent that forms an adduct with CsI (anisole, EtOAc, MeOAc) has a Lewis basic oxygen available for adduct formation as does DEE. However, Cs^+ as a soft acid will preferentially bind to soft bases. Based on the polarizability of the Lewis basic oxygens, the softness decreases according to $\text{MeOAc} \approx \text{EtOAc} > \text{anisole} > \text{DEE}$, thus we expect and see that the antisolvent interaction with CsI follows this trend.^[52] This does not fully explain the removal of bound DMSO as Tol removes as much bound DMSO as EtOAc thus it is likely a combination of multiple factors. In any scenario, the CsI -antisolvent adduct formed is likely driven by significant excess of the antisolvent available to bind rather than thermodynamic favorability. The formation of a CsI -antisolvent adduct correlates with crystallization in the δ - CsPbI_3 phase, regardless of the amount of residual bound DMSO in the as-quenched film. The introduction of the CsI -antisolvent adduct potentially decreases the energetic barriers for direct formation of δ - CsPbI_3 , similar to what has been previously reported in mixed FA/Cs perovskites.^[26] This suggests that the CsI -antisolvent

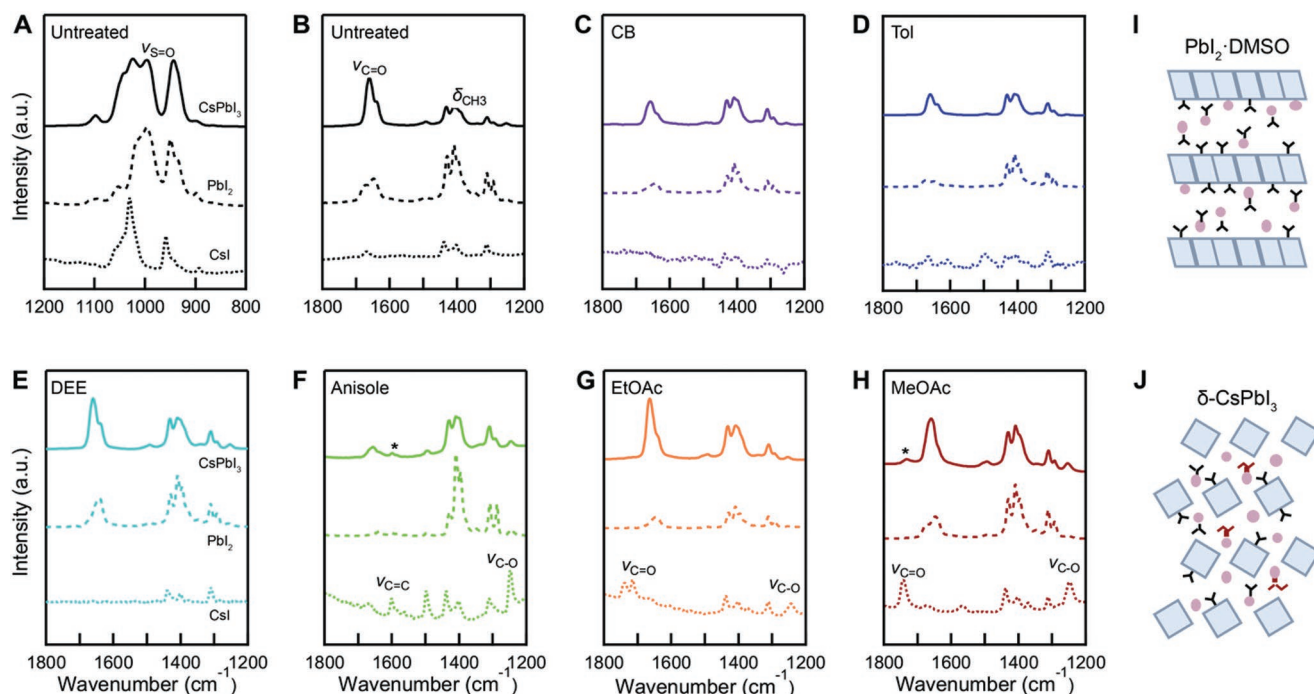


Figure 3. FTIR probing DMSO and antisolvent complexation to CsI (dotted), PbI₂ (dashed) and CsPbI₃ (solid) for A,B) Untreated, C) CB, D) Tol, E) DEE, F) anisole, G) EtOAc and H) MeOAc where * denotes antisolvent peak in CsPbI₃ FTIR spectra. ν denotes a stretching mode and δ is a bending mode. Schematic of I) CsI–DMSO adduct formation in the PbI₂–DMSO crystal structure and J) CsI–MeOAc adduct formation in the δ -CsPbI₃ crystal structure with the PbI₆⁴⁻ octahedra (blue diamonds), Cs (pink circles), DMSO (black chemical structure), and MeOAc (red chemical structure).

adduct influences crystallization more so than the CsI–DMSO or PbI₂–DMSO adduct.

To understand the impact of CsI–antisolvent adduct formation on nucleation, the as-quenched films were annealed at 330 °C for 90 s and the resulting film morphology was captured by scanning electron microscopy (SEM) (Figure 4). All of the yellow as-quenched films (untreated, CB, Tol, DEE) show both areas of large apparent grains and large pinholes, with some needle-like morphologies indicative of PbI₂-dominated growth.^[13,53] There are more needle-like morphologies in films made with CB and Tol, which correlate well with the pre-annealed PbI₂–DMSO crystalline adduct seen in XRD. Although untreated and DEE films were both amorphous as-quenched, the postanneal morphologies are quite different, suggesting that the differences in residual DMSO play a large role in the morphology, as previously demonstrated.^[33] The DEE film has many very large apparent grains (>20 μ m), but also has many large pinholes as compared to the untreated sample. Both large grains and large pinholes are indicative of uncontrolled growth, which likely occurs when the majority of residual bound DMSO is removed via annealing. Anisole, EtOAc and MeOAc all formed an as-quenched crystalline δ -CsPbI₃ film, but with significantly different morphologies. The annealed anisole film appears to nucleate in many places based on the lack of large grains and absence of needle-like morphologies, however the apparent grain domains are small and there are large pinholes. Films made with anisole had a relatively high amount of residual bound DMSO in the as-quenched films, suggesting that higher amounts of residual bound DMSO still retard nucleation and can negatively impact morphology. The

film morphology of both EtOAc and MeOAc shows compact, pinhole free films with large grain domains. The apparent grain boundaries in the EtOAc film are hard to distinguish, but in MeOAc they are clear with grain domains up to \approx 10 μ m large. Only EtOAc and MeOAc films have clean absorbance spectra with minimal scattering backgrounds, whereas all other films show significant scattering backgrounds (Figure S6, Supporting Information). Both EtOAc and MeOAc as-quenched films have the least amount of residual bound DMSO and form the δ -CsPbI₃ crystal phase. The interplay between the crystallization phase, as controlled by the CsI–antisolvent adduct, and the amount of residual bound DMSO or antisolvent at nucleation controls the resulting morphology, demonstrating that both are required for the fabrication of high-quality CsPbI₃ films.

Solar cells were then made with CsPbI₃ prepared using each different antisolvent. MeOAc devices had the highest champion efficiency of 14.4% and an average of 12.95% (Figure 5A). A high J_{SC} of 18.93 mA cm⁻² was achieved due to 88% maximum EQE, although the V_{OC} was slightly low at 0.998 V. This efficiency is respectable for all-inorganic CsPbI₃ devices considering there are no additional organic additives nor HI which may react with DMF and incorporate as DMAI.^[37] CsPbI₃ solar cells made without the use of any additional organic additives have reached a champion efficiency of 15.7% and a recent report of 14.1%, although with organic additives efficiencies of 18.4% have been reported, but the latter are no longer all-inorganic CsPbI₃ devices.^[30,31,36] MeOAc has recently been reported as an effective antisolvent for DMA_{0.1}FA_{0.6}Cs_{0.3}Pb(I_{0.8}Br_{0.2})₃ yielding device efficiencies of 19.2%, suggesting that MeOAc can be effectively used in other Cs-rich perovskites.^[21] EtOAc

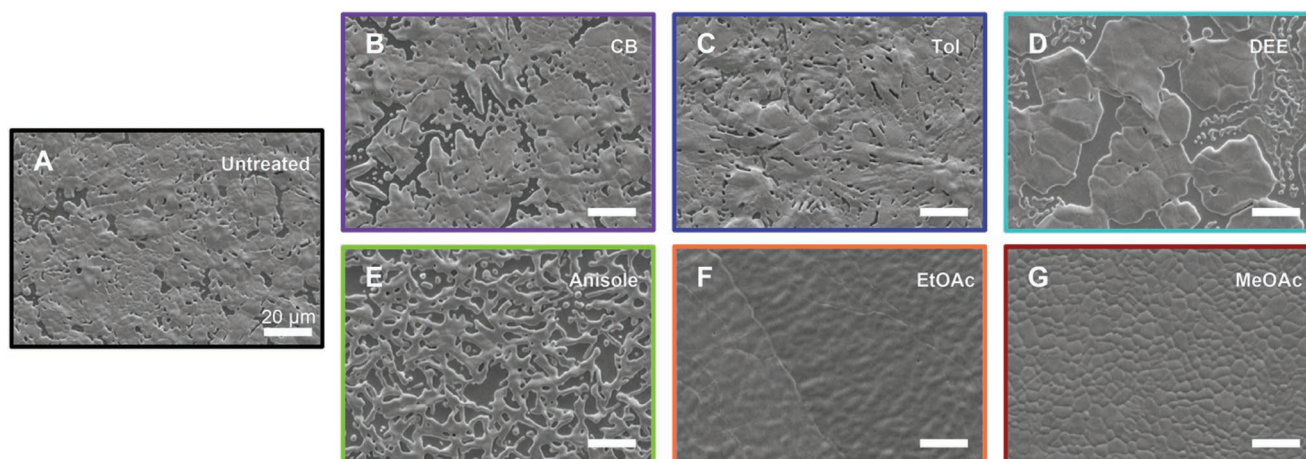


Figure 4. SEM of an annealed film fabricated using each antisolvent treatment, A) Untreated, B) CB, C) Tol, D) DEE, E) Anisole, F) EtOAc, and G) MeOAc with a 20 μm scale bar.

devices reach the second highest PCE of 13.2% although the average was only 9.84% due to large variations in performance influenced by the solvent glovebox atmosphere (Figure 5B and Figures S7 and S8, Supporting Information). EtOAc has also been reported as an effective antisolvent for CsPbI_2Br .^[54] All other antisolvents resulted in champion efficiencies (Figure 5B and Figures S7 and S9, Supporting Information) less than 10%,

due to significant losses in J_{SC} , V_{OC} , and FF. Notably, the third highest performing antisolvent treatment was untreated at a champion efficiency of 9.96%, with a J_{SC} of 17.67 mA cm^{-2} , a V_{OC} of 0.899 V and a FF of 62.7%, demonstrating that the addition of any antisolvent is not necessarily beneficial and can limit device performance. This underscores the importance of understanding the antisolvent mechanism in order to maximize device performance.

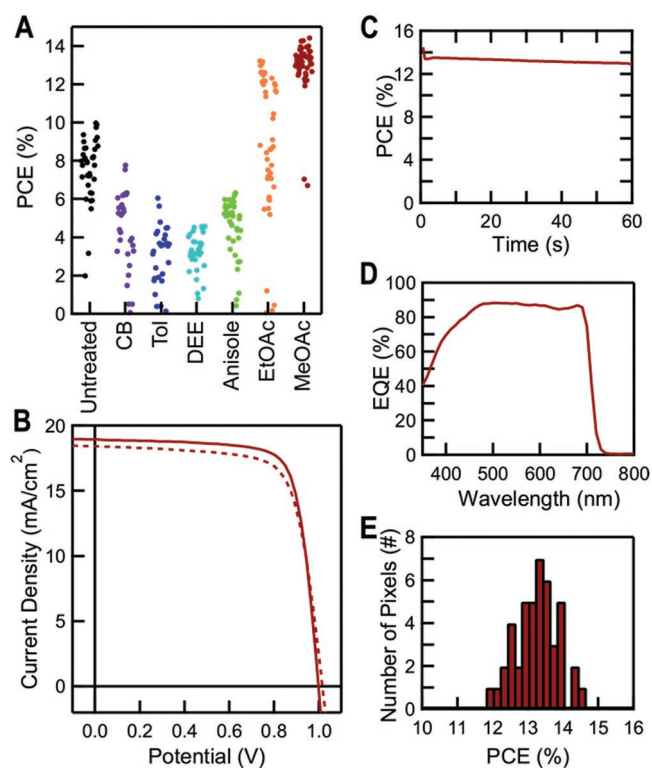


Figure 5. Photovoltaic performance of CsPbI_3 devices. A) PCE distribution for devices made with each antisolvent B) champion JV curve, C) stabilized power output (SPO) as measured by max power point (MPP) tracking D) EQE and E) distribution of efficiencies for 46 devices made with MeOAc.

Clearly, the losses in PCE for the untreated devices as compared to MeOAc are in part due to the large density of pinholes, which allows for contact between the electron and hole transport layers, decreasing V_{OC} and FF by reducing shunt resistance. The large distribution in efficiencies is also due to the poor film coverage, and not to phase degradation (Figure S9, Supporting Information). This is also true for CB, Tol, DEE and anisole. While egregious pinholes do lower J_{SC} , the decrease in absorbance does not fully account for the loss in J_{SC} (Figure S6, Supporting Information). To better understand the optoelectronic properties of antisolvent treated CsPbI_3 films, time-resolved photoluminescence (TRPL) was done (Figure S10, Supporting Information). The TRPL lifetimes for untreated and CB are similar at 1.4 and 2.2 ns respectively, whereas the use of MeOAc triples the lifetime to 6.4 ns, demonstrating that film formation through a CsI–MeOAc adduct results in a film with lower defect density. Although these lifetimes are very short, they are on par with other reported values in similarly performing solar cells.^[31] Second, the normalized EQE was studied, where the relative intensity of the EQE at the band edge compared to the EQE within the bandgap is an indication of the trap state density at the band edge (Figure S11, Supporting Information). This analysis aids in deconvoluting low device efficiency due to large pinholes versus lower material quality. MeOAc maintains 98% of the maximum EQE at the band edge, whereas EtOAc, anisole, and untreated all have similar losses at 90–88%. CB, Tol and DEE have much higher losses at the band edge of 82%, 54%, 69% respectively. These values correlate well with the relative J_{SC} for each antisolvent, demonstrating that the band edge absorption is mainly limiting the J_{SC} . Although CsPbI_3 device operational stability is outside

of the scope of this work, there are many methods used to improve stability which could synergistically be combined with this work to further improve stability.^[34,35,55–58]

3. Conclusions

CsPbI₃ crystallization is not only controlled by the PbI₂–DMSO adduct, but also by the A-site interaction with both DMSO and the antisolvent adduct. The demonstration that CsI, or more generally the A-site cation, can significantly impact nucleation demonstrates the complexity of nucleation and crystallization not previously understood. Here, we have shown in depth exactly how the CsI adducts control nucleation and crystallization and have identified the use of a CsI–antisolvent adduct to promote the nucleation of high-quality films. Specifically, MeOAc quenched films result in devices that are both the highest efficiency at 14.4% and have the lowest standard deviation. MeOAc is also a green, nontoxic solvent. By demonstrating that the antisolvent controls nucleation and crystallization beyond supersaturation for CsPbI₃, we expect that these techniques will be translated to other CsI-rich mixed A-site perovskites and aid in fabricating higher quality wide bandgap perovskites for use in multi-junction perovskite cells and used in conjunction with known methods to improve CsPbI₃ stability.

4. Experimental Section

Materials: All chemicals were used as received. PbI₂ (99.99%) was bought from TCI. SnO₂ colloid precursor (Tin(IV) oxide, 15% in H₂O colloidal dispersion) was purchased from Alfa Aesar. Spiro-OMeTAD was purchased from Lumtec. Tris(2-(1H-pyrazol-1-yl)-4-tert-butylpyridine)cobalt(III)-tris(bis(trifluoromethylsulfonyl)imide): Co[t-BuPyPz]₃[TFSI]₃ (Co-FK209) was purchased from Dyesol. All other chemicals were purchased from Sigma-Aldrich.

CsPbI₃ Film Deposition: Deposition of perovskite was done in a nitrogen glovebox. The precursor solution is a 1 M solution with a 1:1.05 CsI:PbI₂ mole ratio in a 4:1 DMF:DMSO solvent mixture. The solution was vortexed until dissolved and filtered using a 200 nm nylon filter before deposition. The films were deposited by spincoating 45 μ L of solution at 1500 r.p.m. for 45 s and with 10 s of time remaining in the spin procedure 150 μ L of antisolvent was added, unless otherwise specified. When MeOAc or EtOAc were used as the antisolvent the films immediately turn brown. The films were annealed at 330 °C and once the films turn dark brown (after \approx 1 min) they were annealed for another 90 s.

Device Fabrication: Patterned ITO glass was cleaned by sonication in isopropanol and ultraviolet-ozone cleaning for 15 min. A 4:1 (wt/wt) H₂O:SnO₂ nanoparticle solution was spin cast at 3000 r.p.m. for 30 s and then dried at 150 °C for 30 min. Immediately before perovskite deposition, the films were cleaned by ultraviolet-ozone for 15 min. Perovskite deposition was done as detailed above. The Spiro-OMeTAD solution consists of 72 mg mL⁻¹ Spiro-OMeTAD, 28.8 μ L mL⁻¹ tBP, 17.5 μ L LiTFSI stock solution (520 mg mL⁻¹ in acetonitrile) and 5 μ L of Co-FK209 stock solution (300 mg mL⁻¹ in acetonitrile). The Spiro-OMeTAD solution was deposited on top of the perovskite in a nitrogen glovebox by spinning at 5000 r.p.m. for 30 s. 15 nm of MoO_x and 100 nm of Al were thermally evaporated.

Film Characterization: UV–vis of as-quenched samples on glass was done utilizing a Hewlett-Packard 8453 UV–vis spectrophotometer.

For X-ray diffraction, the as-quenched were deposited on quartz substrates. Samples were sealed inside Anton Paar domed sample

holders in a N₂-filled glovebox and measured using a Panalytical X'pert powder diffractometer with Cu anode. Up to four scans were measured and averaged for each film to improve the signal-to-noise. The amorphous background from the polycarbonate dome was subtracted from each pattern.

FTIR measurements were done in an Ar glovebox on a Bruker Alpha FTIR spectrometer using a diffuse reflectance infrared Fourier transform spectrometer (DRIFTS) attachment with a resolution of 4 cm⁻¹. Background measurements were taken on blank substrates and subsequent sample measurements were taken as an average of 24 scans. Spectra were baseline-corrected using the concave rubberband correction method. As quenched films were deposited on gold-coated, polished Si wafer substrates and cycled under vacuum for 9 min before FTIR was taken. A 1 M CsI in 4:1 DMF:DMSO solution and 1 M PbI₂ 4:1 DMF:DMSO solution were used for the as quenched CsI and PbI₂ controls and deposited the same way as CsPbI₃.

Samples for NMR were prepared by fabricating as quenched films on glass slides. The films were then put under vacuum for \approx 3 min to remove any surface adsorbed (unbound) species and then redissolved using deuterated DMSO-*d*₆. A total of five films were used to reach an appropriate concentration. ¹H spectra were recorded using a JEOL ECA-500 at room temperature, and referenced to the absolute integrals of the DMF (7.959–7.936 ppm) and DMSO peaks (singlet, 2.573–2.524 ppm). The raw data was then normalized to the PbI_x solution absorbance, as measured using a Shimadzu UV-3600 ultraviolet–visible–near infrared spectrophotometer. This controls for any variations in solution PbI_x concentration. For ease of comparison, these values for each antisolvent treatment were then compared as a percent of residual DMSO in the untreated film.

SEM was done on annealed films in a Hitachi S-4800 field emission scanning electron microscope.

Time-resolved photoluminescence (TRPL) films were measured using a supercontinuum fiber laser (NKT Photonics, Super K) operating at 5 MHz as the excitation source. Films were excited at 500 nm at a low fluence ($\ll 10^{15}$ s⁻¹) and a Hamamatsu C10910–04 streak camera was used to collect time-resolved spectra. Bi-exponential fits of the TRPL decays were weighted to calculate the average PL lifetime using the equation: $\tau_{\text{avg}} = (A_0\tau_0 + A_1\tau_1)/(A_0 + A_1)$.

Device Characterization: Devices were tested in a nitrogen glovebox using a Newport Oriel Sol3A solar simulator with a xenon lamp where the intensity was calibrated to 100 mW cm⁻² AM1.5G using a KG2 filtered NREL-certified mono-Si reference solar cell. JV scans were taken from forward bias to reverse bias with the following scan parameters at a scan rate of 0.51 V s⁻¹ with a step size of 23 mV. The devices were \approx 0.1 cm² and were masked with a metal aperture to define an active area of 0.058 cm². Stable power output (SPO) was measured by recording the current output when the illuminated device was held at a constant voltage near the maximum power point of the JV scan. Maximum power point (MPP) tracking was measured similarly, but the voltage was allowed to float. EQE measurements were taken using a Newport Oriel IQE2.

Supporting Information

Supporting Information is available from the Wiley Online Library or from the author.

Acknowledgements

This work was authored in part by the Alliance for Sustainable Energy, Limited Liability Company, the manager and operator of the National Renewable Energy Laboratory under Contract No. DE-AC36-08G028308. The views expressed in the article do not necessarily represent the views of the Department of Energy or the U.S. Government. T.M., A.H., and J.M.L. acknowledge the Operational Energy Capability Improvement Fund of the Department of Defense. S.N.H. acknowledges support from

the NREL directors fellowship LDRD program. L.M.W. acknowledges support from the Building Technologies Offices within the U.S. Department of Energy Office of Energy Efficiency and Renewable Energy. T.H.S. acknowledges the Department of Chemistry at the Colorado School of Mines for financial support through teaching assistantships and a Graduate Research Fellowship award. C.C.B. and M.D.M. acknowledge support from the National Science Foundation Graduate Research Fellowship under Grant No. DGE-1656518. A.R.M. and H.J.S. have received funding from the Strategic University Network to Revolutionise Indian Solar Energy (SUNRISE), an EPSRC grant number EP/P032591/1. D.R.D. acknowledges the U.S. DOE, Office of Science, Office of Workforce Development for Teachers and Scientists, Science Undergraduate Laboratory Internship (SULI) Program for funding in 2018 and 2019.

Conflict of Interest

The authors declare no conflict of interest.

Keywords

acid–base complex, adduct, antisolvent, CsPbI₃, perovskite, solar cells

Received: October 14, 2019

Revised: January 8, 2020

Published online: January 31, 2020

- [1] "NREL Best Research-Cell Efficiencies Chart," <https://www.nrel.gov/pv/assets/pdfs/best-research-cell-efficiencies.20190802.pdf>, (accessed: August 2019).
- [2] Q. Jiang, Y. Zhao, X. Zhang, X. Yang, Y. Chen, Z. Chu, Q. Ye, X. Li, Z. Yin, J. You, *Nat. Photonics* **2019**, *13*, 460.
- [3] Y. Rong, Y. Hu, A. Mei, H. Tan, M. I. Saidaminov, S. Il Seok, M. D. McGehee, E. H. Sargent, H. Han, *Science* **2018**, *361*, eaat8235.
- [4] Z. Li, T. R. Klein, D. H. Kim, M. Yang, J. J. Berry, M. F. A. M. Van Hest, K. Zhu, *Nat. Rev. Mater.* **2018**, *3*, 18017.
- [5] N. J. Jeon, J. H. Noh, Y. C. Kim, W. S. Yang, S. Ryu, S. Il Seok, *Nat. Mater.* **2014**, *13*, 897.
- [6] M. Saliba, T. Matsui, J.-Y. Seo, K. Domanski, J.-P. Correa-Baena, M. K. Nazeeruddin, S. M. Zakeeruddin, W. Tress, A. Abate, A. Hagfeldt, M. Gratzel, *Energy Environ. Sci.* **2016**, *9*, 1989.
- [7] J. Tong, Z. Song, D. Hoe Kim, X. Chen, C. Chen, A. F. Palmstrom, P. F. Ndione, M. O. Reese, S. P. Dunfield, O. G. Reid, J. Liu, F. Zhang, S. P. Harvey, Z. Li, S. T. Christensen, G. Teeter, D. Zhao, M. M. Al-Jassim, M. F. A. M. van Hest, M. C. Beard, S. E. Shaheen, J. J. Berry, Y. Yan, K. Zhu, *Science* **2019**, *364*, 475.
- [8] Y. Zhou, O. S. Game, S. Pang, N. P. Padture, *J. Phys. Chem. Lett.* **2015**, *6*, 4827.
- [9] M. Jung, S.-G. Ji, G. Kim, S. Il Seok, *Chem. Soc. Rev.* **2019**, *48*, 2011.
- [10] G. E. Eperon, V. M. Burlakov, P. Docampo, A. Goriely, H. J. Snaith, *Adv. Funct. Mater.* **2014**, *24*, 151.
- [11] K. Meng, L. Wu, Z. Liu, X. Wang, Q. Xu, Y. Hu, S. He, X. Li, T. Li, G. Chen, *Adv. Mater.* **2018**, *30*, 1706401.
- [12] W. Van Schalkwijk, *Nat. Mater.* **2015**, *348*, 366.
- [13] S. Paek, P. Schouwink, E. N. Athanasopoulou, K. T. Cho, G. Grancini, Y. Lee, Y. Zhang, F. Stellacci, M. K. Nazeeruddin, P. Gao, *Chem. Mater.* **2017**, *29*, 3490.
- [14] N. Sakai, S. Pathak, H. Chen, A. A. Haghighirad, S. D. Stranks, T. Miyasaka, H. J. Snaith, *J. Mater. Chem. A* **2016**, *4*, 4464.
- [15] K. Bruening, C. J. Tassone, *J. Mater. Chem. A* **2018**, *6*, 18865.
- [16] K. Wang, M. Tang, H. X. Dang, R. Munir, D. Barrit, M. De Bastiani, E. Aydin, D. Smilgies, S. De Wolf, A. Amassian, *Adv. Mater.* **2019**, *31*, e1808357.
- [17] M. Yang, Z. Li, M. O. Reese, O. G. Reid, D. H. Kim, S. Siol, T. R. Klein, Y. Yan, J. J. Berry, M. F. A. Van Hest, K. Zhu, *Nat. Energy* **2017**, *2*, 17038.
- [18] J. A. Christians, P. Schulz, J. S. Tinkham, T. H. Schloemer, S. P. Harvey, B. J. T. de Villers, A. Sellinger, J. J. Berry, J. M. Luther, *Nat. Energy* **2018**, *3*, 68.
- [19] M. Stollerfoht, C. M. Wolff, J. A. Márquez, S. Zhang, C. J. Hages, D. Rothhardt, S. Albrecht, P. L. Burn, P. Meredith, T. Unold, D. Neher, *Nat. Energy* **2018**, *3*, 847.
- [20] R. E. Beal, D. J. Slotcavage, T. Leijtens, A. R. Bowring, R. A. Belisle, W. H. Nguyen, G. F. Burkhard, E. T. Hoke, M. D. McGehee, *J. Phys. Chem. Lett.* **2016**, *7*, 746.
- [21] A. F. Palmstrom, G. E. Eperon, T. Leijtens, R. Prasanna, S. N. Habisreutinger, W. Nemeth, E. A. Gaubling, S. P. Dunfield, M. Reese, S. Nanayakkara, T. Moot, J. Werner, J. Lui, B. To, S. T. Christensen, M. D. McGehee, M. F. A. M. Van Hest, J. M. Luther, J. J. Berry, D. T. Moore, *Joule* **2019**, *3*, 2193.
- [22] K. A. Bush, A. F. Palmstrom, Z. J. Yu, M. Boccard, R. Cheacharoen, J. P. Mailoa, D. P. McMeekin, R. L. Z. Hoye, C. D. Bailie, T. Leijtens, I. M. Peters, M. C. Minichetti, N. Rolston, R. Prasanna, S. Sofia, D. Harwood, W. Ma, F. Moghadam, H. J. Snaith, T. Buonassisi, Z. C. Holman, S. F. Bent, M. D. McGehee, *Nat. Energy* **2017**, *2*, 17009.
- [23] D. P. McMeekin, G. Sadoughi, W. Rehman, G. E. Eperon, M. Saliba, M. T. Hörantner, A. Haghighirad, N. Sakai, L. Korte, B. Rech, M. B. Johnston, L. M. Herz, H. J. Snaith, *Science* **2016**, *351*, 151.
- [24] E. T. Hoke, D. J. Slotcavage, E. R. Dohner, A. R. Bowring, H. I. Karunadasa, M. D. McGehee, *Chem. Sci.* **2015**, *6*, 613.
- [25] G. Zhou, J. Wu, Y. Zhao, Y. Li, J. Shi, Y. Li, H. Wu, D. Li, Y. Luo, Q. Meng, *ACS Appl. Mater. Interfaces* **2018**, *10*, 9503.
- [26] M. Qin, K. Tse, T. Lau, Y. Li, C. Su, G. Yang, J. Chen, J. Zhu, U. Jeng, G. Li, H. Chen, X. Lu, *Adv. Mater.* **2019**, *31*, e1901284.
- [27] A. Hazarika, Q. Zhao, E. A. Gaubling, J. A. Christians, B. Dou, A. R. Marshall, T. Moot, J. J. Berry, J. C. Johnson, J. M. Luther, *ACS Nano* **2018**, *12*, 10327.
- [28] Z. Li, M. Yang, J. Park, S. Wei, J. J. Berry, K. Zhu, *Chem. Mater.* **2016**, *28*, 284.
- [29] C. Yi, J. Luo, S. Meloni, A. Boziki, N. Ashari-Astani, C. Gratzel, S. M. Zakeeruddin, U. Rothlisberger, M. Gratzel, *Energy Environ. Sci.* **2016**, *9*, 656.
- [30] P. Wang, X. Zhang, Y. Zhou, Q. Jiang, Q. Ye, Z. Chu, X. Li, X. Yang, Z. Yin, J. You, *Nat. Commun.* **2018**, *9*, 2225.
- [31] C. Fai, J. Lau, Z. Wang, N. Sakai, J. Zheng, C. H. Liao, M. Green, S. Huang, H. J. Snaith, A. Ho-Baillie, *Adv. Energy Mater.* **2019**, *9*, 1901685.
- [32] P. Luo, W. Xia, S. Zhou, L. Sun, J. Cheng, C. Xu, Y. Lu, *J. Phys. Chem. Lett.* **2016**, *7*, 3603.
- [33] A. J. Ramadan, L. A. Rochford, S. Fearn, H. J. Snaith, *J. Phys. Chem. Lett.* **2017**, *8*, 4172.
- [34] Y. Wang, T. Zhang, M. Kan, Y. Zhao, *J. Am. Chem. Soc.* **2018**, *140*, 12345.
- [35] Y. Wang, T. Zhang, Y. Wang, T. Zhang, M. Kan, Y. Li, T. Wang, Y. Zhao, *Joule* **2018**, *2*, 1.
- [36] Y. Wang, M. I. Dar, L. K. Ono, T. Zhang, M. Kan, Y. Li, L. Zhang, X. Wang, Y. Yang, X. Gao, Y. Qi, M. Gratzel, Y. Zhao, *Science* **2019**, *365*, 591.
- [37] W. Ke, I. Spanopoulos, C. C. Stoumpos, M. G. Kanatzidis, *Nat. Commun.* **2018**, *9*, 4785.
- [38] N. Ahn, D.-Y. Son, I.-H. Jang, S. M. Kang, M. Choi, N. Park, *J. Am. Chem. Soc.* **2015**, *137*, 8696.
- [39] E. D. Risberg, J. Mink, A. Abbasi, M. Y. Skripkin, L. Hajba, P. Lindqvist-Reis, E. Bencze, M. Sandstr, *Dalton Trans.* **2008**, 1328.

- [40] Y. Jo, K. S. Oh, M. Kim, K. Kim, H. Lee, C. Lee, D. S. Kim, *Adv. Mater. Interfaces* **2016**, *3*, 1500768.
- [41] J. Stevenson, B. Sorenson, V. H. Subramaniam, J. Raiford, P. P. Khlyabich, Y. Loo, P. Clancy, *Chem. Mater.* **2017**, *29*, 2435.
- [42] J. C. Hamill, J. Schwartz, Y. Loo, *ACS Energy Lett.* **2018**, *3*, 92.
- [43] N. R. Babij, E. O. Mccusker, G. T. Whiteker, B. Canturk, N. Choy, L. C. Creemer, C. V De Amicis, N. M. Hewlett, P. L. Johnson, J. A. Knobelsdorf, F. Li, B. A. Lorsbach, B. M. Nugent, S. J. Ryan, M. R. Smith, Q. Yang, *Org. Process Res. Dev.* **2016**, *20*, 661.
- [44] C. M. Hansen, in *The Three Dimensional Solubility Parameter and Solvent Diffusion Coefficient*, Danish Technical Press, Copenhagen **1967**, pp. 13–30.
- [45] F. Cataldo, *Eur. Chem. Bull* **2015**, *4*, 92.
- [46] A. Hadi, B. J. Ryan, R. D. Nelson, K. Santra, F. Y. Lin, E. W. Cochran, M. G. Panthani, *Chem. Mater.* **2019**, *31*, 4990.
- [47] Y. Zong, Z. Zhou, M. Chen, N. P. Padture, Y. Zhou, *Adv. Energy Mater.* **2018**, *8*, 1800997.
- [48] D. Zhang, S. W. Eaton, Y. Yu, L. Dou, P. Yang, *J. Am. Chem. Soc.* **2015**, *137*, 9230.
- [49] J. K. Wilmshurst, *J. Mol. Spectrosc.* **1957**, *1*, 201.
- [50] L. M. Wheeler, E. M. Sanehira, A. R. Marshall, P. Schulz, M. Suri, N. C. Anderson, J. A. Christians, D. Nordlund, D. Sokaras, T. Kroll, S. P. Harvey, J. J. Berry, L. Y. Lin, J. M. Luther, *J. Am. Chem. Soc.* **2018**, *140*, 10504.
- [51] A. Swarnkar, A. R. Marshall, E. M. Sanehira, B. D. Chernomordik, D. T. Moore, J. A. Christians, T. Chakrabarti, J. M. Luther, *Science* **2016**, *354*, 92.
- [52] R. G. Pearson, *J. Am. Chem. Soc.* **1963**, *85*, 3533.
- [53] J. Cao, X. Jing, J. Yan, C. Hu, R. Chen, J. Yin, J. Li, N. Zheng, *J. Am. Chem. Soc.* **2016**, *138*, 9919.
- [54] C. Dong, X. Han, Y. Zhao, J. Li, L. Chang, W. Zhao, *Sol. RRL* **2018**, *2*, 1800139.
- [55] T. Zhang, M. I. Dar, G. Li, F. Xu, N. Guo, M. Grätzel, Y. Zhao, *Sci. Adv.* **2017**, *3*, 2.
- [56] Y. Fu, M. T. Rea, J. Chen, D. J. Morrow, M. P. Hautzinger, Y. Zhao, D. Pan, L. H. Manger, J. C. Wright, R. H. Goldsmith, S. Jin, *Chem. Mater.* **2017**, *29*, 8385.
- [57] B. Li, Y. Zhang, L. Fu, T. Yu, S. Zhou, L. Zhang, L. Yin, *Nat. Commun.* **2018**, *9*, 1076.
- [58] Q. Wang, X. Zheng, Y. Deng, J. Zhao, Z. Chen, J. Huang, *Joule* **2017**, *1*, 371.